Powder Met2024 AMPM 2024
JUNE 16–19 • PITTSBURGH

NIOBIUM (NB) BASE ALLOY POWDERS FOR HIGH-TEMPERATURE ADDITIVE MANUFACTURING APPLICATIONS

Bahar Fayyazi,* Shaumik Lenka, Thomas Wagstaff,*** Adrien Rapoport,***, Nicholas Sim,*** and Markus Weinmann******

The development of commercially available niobium (Nb) base alloy powders for additive manufacturing (AM) opens completely new opportunities to produce high-temperature, high-performance components that are particularly interesting for aerospace applications. It is crucial to comprehend the entire workflow, which ranges from powder production and characterization to the determination of optimal process parameters. Insights into the preparation, characterization, and processing of Nb-base alloy powders using metal AM techniques are presented in detail. Nb-base alloys such as C-103 and FS-85 are emerging as promising candidates to improve the capabilities of additive manufacturing, particularly in aerospace applications. What sets Nb-base alloys apart from common materials are their exceptional properties—remarkably low density combined with high thermal conductivity, and outstanding mechanical strength at high temperatures. These properties make such alloys a superior alternative to traditional Ni- and Co-base materials, particularly in environments with temperatures surpassing 1,050 °C. While C-103 has become firmly established in conventional manufacturing, there is still no experience with conventional molding for FS-85, which is currently the focus of interest due to its extraordinary strength at elevated temperatures. The commercial availability of FS-85 alloy powders for additive manufacturing opens exciting possibilities for producing high-performance components with complex geometries.

Presented at PowderMet2024 and published in Advances in Powder Metallurgy & Particulate Materials—2024, proceedings of the 2024 International Conference on Powder Metallurgy & Particulate Materials are available from the Publications Department of MPIF www.mpif.org.

INTRODUCTION

Refractory metals are characterized by very high melting temperatures and therefore have the potential to be used in future aerospace applications. The maximum operating temperature of Ni- or Co-based superalloys currently applied in engines is approx. 1,050 °C. Above this temperature, these materials are no longer structurally stable due to the onset of creep.

In contrast, high temperature refractory metals, i.e., Hf, Nb, Ta, Mo, and W possess melting temperatures in the range of 2,200 °C (Hf) and 3,400 °C (W) and thus have the potential to perform at temperatures far exceeding 1,050 °C. The pure metals as well as their alloys are accordingly outperforming even the most advanced Ni- and Co-based superalloys. Among the refractory metals, Nb is the most attractive candidate for application in structurally and thermally-loaded parts because of its favorable combination of high melting point (2,477 °C), relatively low density (8.57 g/cm^3), good thermal conductivity (54 W/m·K), and ductility.

Intensive studies on Nb-base alloys already started in the 1960s and 1970s, mostly triggered by the search of Boeing and NASA for new aircraft and aerospace alloys, i.e., for use in turbine and propulsion systems. In most cases, Nb was alloyed with other refractory metals, such as the metals mentioned previously, to improve high-temperature properties and allow higher operating temperatures of the manufactured parts. The most prominent alloys to mention in this regard are (in alphabetical order) C-103 (Nb-10Hf-1Ti),[1] Cb-129Y (Nb-10W-10Hf-0.1Y),[2] Cb-752 (Nb-10W-2.5Zr),[3] FS-85 (Nb-28Ta-10W-1Zr),[4] Nb-1Zr,[5] and WC-3009 (Nb-30Hf-9W).[6] In addition, several reviews appeared comparing room and high-temperature properties of the Nb-base alloys.[7–10]

Because of the difficult machinability of Nb-base alloys, and as ingot production is expensive, applications have until recently been limited to simple shapes, e.g., products made from sheet and bar such as expansion chamber skirts made from TIG welded sheet. Realizing complex shapes is challenging due to the high hot working temperature of Nb-base alloys. Among Nb-base

*Product Manager Metal Powders, ****Senior Scientist Technology Scout, TANIOBIS GmbH, Im Schleeke 78-91, 38642 Goslar, Germany; Email: Bahar.Fayyazi@taniobis.com, **Senior Alloy Design Engineer, ***Alloy Design Engineer, Alloyed Ltd.,15 Oxford Industrial Park, Oxford, OX5 1QU, UK

TABLE I. CHEMICAL COMPOSITION (wt.%) AND PARTICLE-SIZE-DISTRIBUTION, I.E., D_{10}, D_{50}, D_{90} (µm) VALUES OF C-103 AND FS-85 POWDERS

	Nb	Hf	Ti	Zr	Ta	W	O	N	D_{10}	D_{50}	D_{90}
C-103	89.3	9.0	0.9	0.1 <	0.116	n.d.	0.029	0.004	17	30	54
FS-85	62.1	< 0.01	n.d.	0.9	28.7	10.0	0.046	0.004	17	31	53

alloys, C-103 has been the most popular, since it possesses the best compromise between strength and processability.

In the last decade, near-net-shape, i.e., AM processes were developed at a rapid pace as economic alternatives to classical processing such as casting, forging, and (subtractive) machining. Typical AM processes applicable for Nb and Nb-base alloys in powder form are laser powder-bed-fusion (PBF-LB),[11–13] electron beam powder bed fusion (PBF-EB),[14,15] or directed energy deposition (DED).[16,17] These technologies offer significant advantages over conventional processing, including cost-effective part production through more efficient material utilization and the capability to manufacture complex components.

In the present paper, we report on the additive manufacturing using laser powder-bed-fusion of Nb-base alloys C-103, as a widely manufactured alloy, and FS-85, which was first additively manufactured by our group.

Detailed insights are provided on the manufacture and characterization of suitable prealloyed starting powders, the development of AM processes using different equipment from single to 4-laser printer, and detailed investigations on microstructure and mechanical properties of additively manufactured C-103 and FS-85 parts.

Powder Production and Characterization

Spherical C-103 and FS-85 powders were obtained from prealloyed electrodes by electrode induction melting gas atomization (EIGA) conducted under a purified argon (4.6, Linde) atmosphere. The chemical compositions of the powders determined by inductively coupled plasma optical emission spectroscopy (ICP-OES; Analytik Jena PlasmaQuant PQ 9000/9100), carrier gas hot extraction (LECO TCH-600/ONH-836), and/or combustion analysis (LECO CS-744) are listed in Table I. As-atomized powders were sieved using 150 µm mesh screens and then transferred into an air classifier for deagglomeration and removal of fine particles (< 15 µm) to improve flow properties. From the remaining powders, the PBF-LB particle size fraction (15–63 µm) was extracted by ultrasonic sieving with 63 µm meshes. Particle-size-distributions (PSD, Table I provides D_{10}, D_{50}, and D_{90} values) were determined using a Master Sizer 2000 (Malvern, Worcestershire, United Kingdom).

X-ray diffraction was conducted on powders with Cu Kα radiation in a 2θ range between 10 and 80° to assess the phase structure using a Panalytical X-ray diffractometer (Almelo, Overijssel, Netherlands; X'Pert MPD-PRO, Cu Kα radiation). For comparison, pure Nb powders were also investigated. Indexing of the diffractograms was performed using the ICDD pdf-2 database.[18] The XRD patterns of C-103 and FS-85 shown in Figure 1 are identical to that of Nb, exhibiting the typical 110, 200, and 211 ß-phase reflections, indicating that the prealloyed powders have a bcc structure, similar to Nb.

Scanning electron microscopy (SEM) including energy dispersive X-ray spectroscopy (EDS) and electron backscatter diffraction (EBSD) were employed to investigate the microstructure of powders and built parts. EDS analysis was conducted on both polished powder particle cross-sections as well as additively manufactured specimens (next section) to assess their local and global (average) chemical compositions. For EBSD, specimens were mechanically ground and electropolished for 35 s at 30 V and 1.1 A using A3 electrolyte (Struers).

SEM, BSE, EDS, and EBSD images of C-103 and FS-85 powders are compared in Figure 2. The results of the EDS measurements are provided in Table II. Application in powder bed additive manufacturing processes requires good processability, particularly flowability of the powder feedstock. A spherical shape is highly advantageous to guarantee free-flow and achieving a uniformly distributed powder bed in each individual coating step. Moreover, the absence of smaller particles and agglomerates improves flow properties. Pores or voids in the powders must be avoided to suppress inclusion of porosity in the additively manufactured parts. According to Figure 1 both C-103 and FS-85 powder

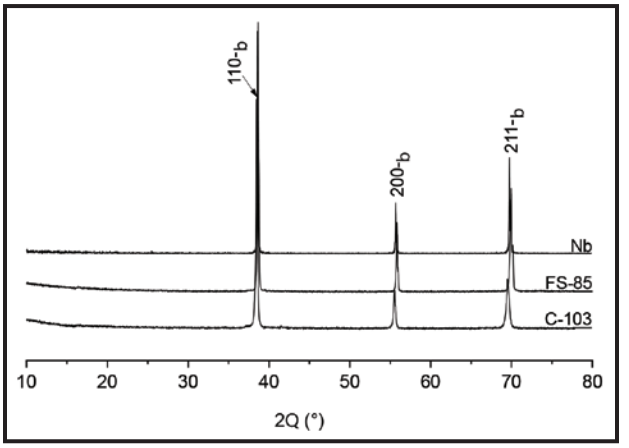

Figure 1. *XRD diagrams of C-103 as well as FS-85 powders and comparison with Nb*

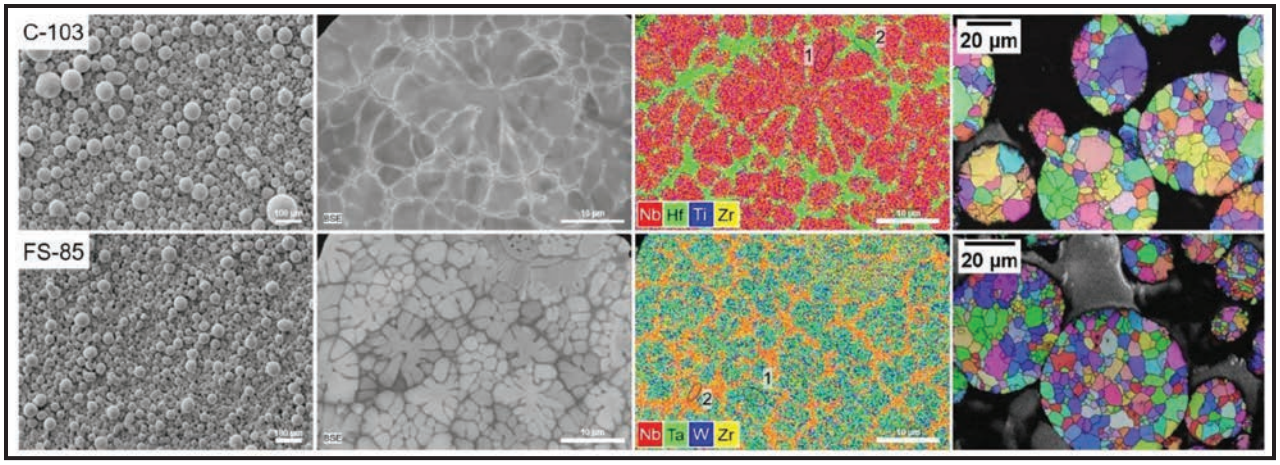

Figure 2. *SEM, BSE, EDS and EBSD (from left to right) of C-103 (top row) and FS-85 (bottom row). The chemical compositions of spots 1 and 2 and of the entire particle in the EDS are provided in Table II*

TABLE II. CHEMICAL COMPOSITION (wt.%) OF C-103 AND FS-85 POWDERS DETERMINED BY EDX

	EDS	Nb	Hf	Ti	Zr	Ta	W
C-103	Σ	87.2	11.7	0.5	0.7	—	—
	Spot 1	92.1	6.9	0.0	1.0	—	—
	Spot 2	78.9	19.7	0.2	1.3	—	—
FS-85	Σ	61.7	—	—	2.3	26.3	9.8
	Spot 1	61.2	—	—	2.0	26.7	10.1
	Spot 2	68.2	—	—	4.9	21.1	5.8

particles exhibit perfectly spherical shapes. They are not agglomerated and have no satellites, i.e., small particles fused on the powder particle surfaces. Likewise, there is no evidence of particle agglomeration. The BSE micrographs indicate two important facts: on one hand, there are no pores in the particles and, on the other, both materials form dendritic microstructures. The local and overall chemical composition of the particles can be derived from EDS shown in Figure 2. The results listed in Table II compare the compositions of the entire particle with that of the dendrite (spots 1) and interdendritic features (spots 2). In both materials, significant deviations in the chemical composition of dendritic and interdendritic phases are observed.

Assessment of the local composition within the individual specimens reveals differences for the dendritic and interdendritic regions. In C-103, Nb appears enriched in the dendritic phase whereas Hf is enriched in the interdendritic phase. According to Table II dendritic features are composed of 92.1 wt.% Nb and 6.9 wt.% Hf whereas the interdendritic phase consists of 78.9 wt.% Nb and 19.7 wt.% Hf. The average particle composition is 90.9 wt.% Nb and 7.9 wt.% Hf. Likewise, there are pronounced differences in the chemical composition of dendritic and interdendritic features in FS-85. While the first is enriched in Ta (26.7 compared with 21.1 wt.%) and W (10.1 compared with 5.8 wt.%) the latter is enriched in Nb (68.2 compared with 61.2 wt.%) and Zr (4.9 compared with 2.0 wt.%).

The appearance of the dendritic-type solidification microstructures in powders is most probably related to the inherent cooling rates during EIGA, which are not sufficiently high to prevent all segregation processes.

Solidification, preferably taking place at the solid/liquid interface, causes preferential crystallization of the metals with higher melting points. As a result, niobium (melting point 2,477 °C) in C-103 enriches in the dendrite phase, whereas Hf (melting point 2,227 °C) enriches the interdendritic phase. Similarly, the dendritic phase in FS-85 is enriched in W (melting point 3,422 °C) and Ta (melting point 3,020 °C) whereas the interdendritic phase is enriched in Nb and Zr (melting point 1,855 °C). Such observations are often reported for other high-alloy materials composed of elements with significant differences in their melting points, e.g., gas-atomized Ti-42Nb,[19] or Ti/Ta/Al alloys.[20] It will be discussed subsequently that the microstructures of the additively manufactured C-103 and FS-85 specimens do not comprise such dendritic features. The reason is the very high cooling rate of 1 – 40 °C/µs in the PBF-LB processes, which avoids diffusion processes during solidification thus forming microstructures with an extremely homogeneous distribution of all constituent elements.[21]

EBSD studies of C-103 and FS-85 powders (Figure 2) provide information on crystal sizes, structure, and orientation. It is evident that the crystal sizes and shapes in both materials roughly correspond to those of the dendritic structures, seen in the BSE images. In addition, the crystals are oriented randomly; a preferred orientation cannot be recognized. This is likewise very different from additively manufactured structures that in general possess highly anisotropic structures—formation of columnar structures in the build direction.

Additive Manufacturing Preliminary Infill Parameter Development Using Single Laser Renishaw AM400

Build studies on C-103 and FS-85 were performed by laser beam powder-bed-fusion (PBF-LB) in a protective Ar atmosphere using a Renishaw AM400 system, equipped with a 1075 nm fiber laser system. Initially, the general processability was investigated by building individual melt tracks with different parameter settings to obtain information about the thickness and depth of the melt-pool. Such information is mandatory to ensure overlap of the melt pools and to avoid pore formation in the built parts due to lack of fusion. On the other hand, keyhole formation caused by trapped vapor within the melt pool, is a detrimental defect, which occurs due to excessive energy input. Accordingly, a process window must be determined individually for every single alloy composition and powder/equipment combination. An example of a DOE of FS-85 for single-track printing using a laser power of 300 or 400 W and exposure times of 50–90 µs is shown in Figure 3, and the result of the corresponding experiment performed on the previously mentioned AM 400 metal additive manufacturing system.

The single lines were analyzed metallographically to evaluate their quality in terms of track stability. For this purpose, the scan track width and the one-dimensional (1D) energy density were calculated and plotted against each other and compared with the quality of the printed line, which was investigated using metallographic analysis.

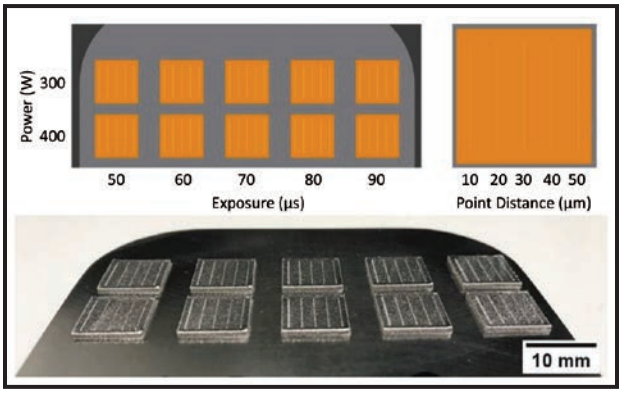

Figure 3. *Single Track DOE (top) and experiments of FS-85*

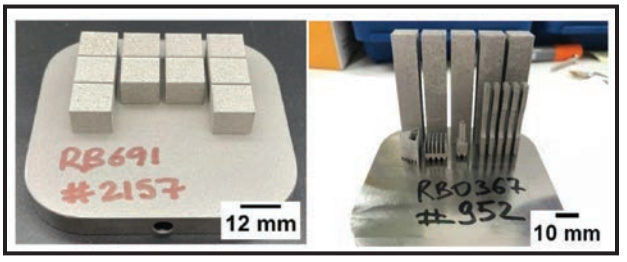

Figure 4. *PBF-LB -manufactured C-103 test cubes (left) for optical density determination and various test bars (right) for tensile tests, high temperature tests, and complex thin-wall build performance*

The process parameters were further refined by building test cubes measuring 10 by 10 by 10 mm^3 (Figure 4). These were used to determine the influence of the build parameters on the quality of the built parts applying optical density measurements. In addition, they were used to examine the microstructure of the as-built parts by means of electron microscopy. To explore the limits of the process and the processability of the powders, a series of components with more complex geometry was also built.

Systematic correlation of energy input with respect to volumetric energy density and residual porosity has been performed for both, C-103 and FS-85. A series of 20 optical micrographs taken from additively manufactured C-103 cubes (out of 52) using different printing parameters is shown in Figure 5. The dependence of porosity and volumetric energy density (VED) is illustrated graphically in Figure 6 for C-103 and FS-85 alloys.

The cross-sections displayed show optical densities between 99.1% in the worst case and 99.9% in the best case. In terms of porosity, this represents an enormous improvement, as the corresponding porosity values could be reduced from about. 1% to approximately 0.06%. Interestingly, there are no signs indicating lack of fusion porosity in any of the micrographs. Only pores with spherical geometry, typical for gas porosity, are observed.

The graphical representation of these results in Figure 6 points to the fact that the range of build parameters suitable for PBF-LB of C-103 is relatively broad. At the low end, the VED is about 160 J/mm^3 whereas the maximum energy input should not exceed 240 J/mm^3. The process window for FS-85, which is also depicted in Figure 6, is smaller. Although this alloy contains high-melting elements tantalum (melting point 3,020 °C, 28,7 wt.%) and tungsten (melting point 3,422 °C, 10 wt.%), the required VED to build dense specimens ranges from 105–125 J/mm^3 and is thus significantly lower than for C-103.

Independent of the applied parameters, the additive manufacturing process has a significant impact on the microstructure development. It has frequently been reported that PBF-LB results in highly anisotropic microstructures with elongated columnar grains oriented in the building direction (BD).[22,23] Figure 7 presents a BSE image of PBF-LB-processed FS-85, indicating that not only the microstructure but the chemical composition is also affected by the additive manufacturing process.

The BSE image in Figure 7, taken perpendicular to the

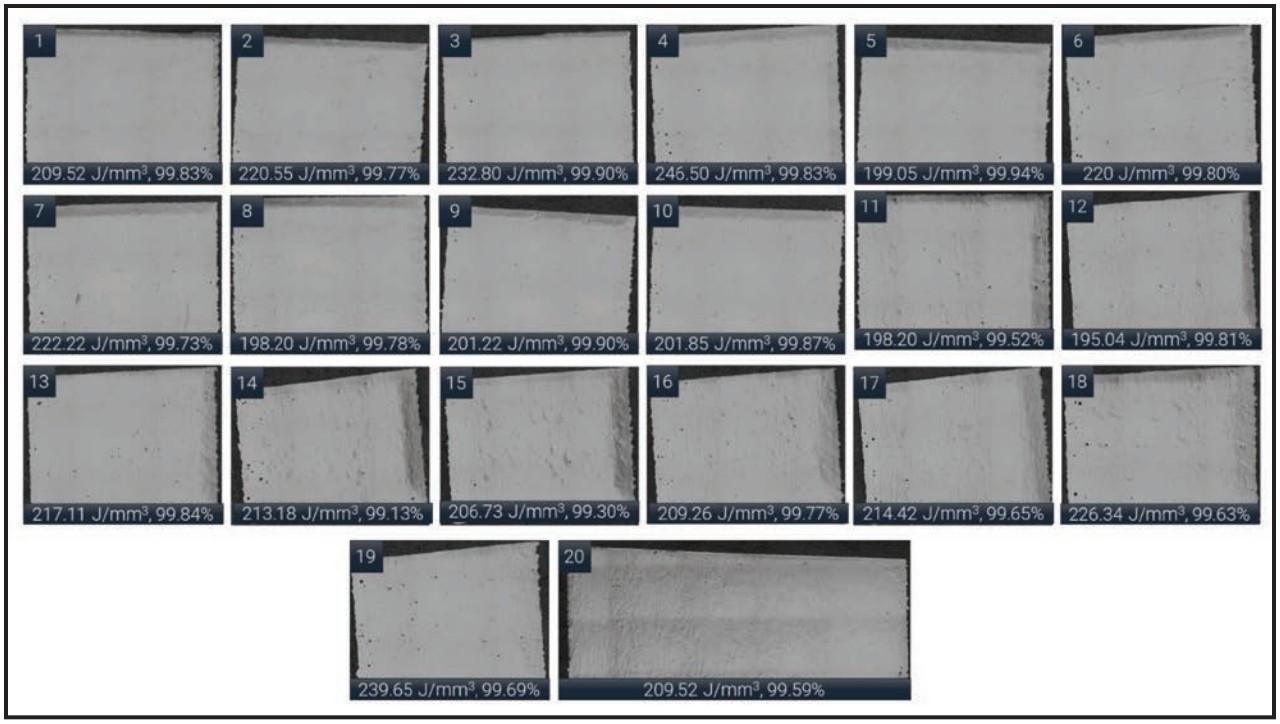

Figure 5. *Light microscopy (LM) images of polished of XZ cross sections of as-built 10 by 10 by 10 mm³ C-103 test cubes using the AM400 system illustrating the influence of energy input in the PBF-LB processing on (relative) optical density*

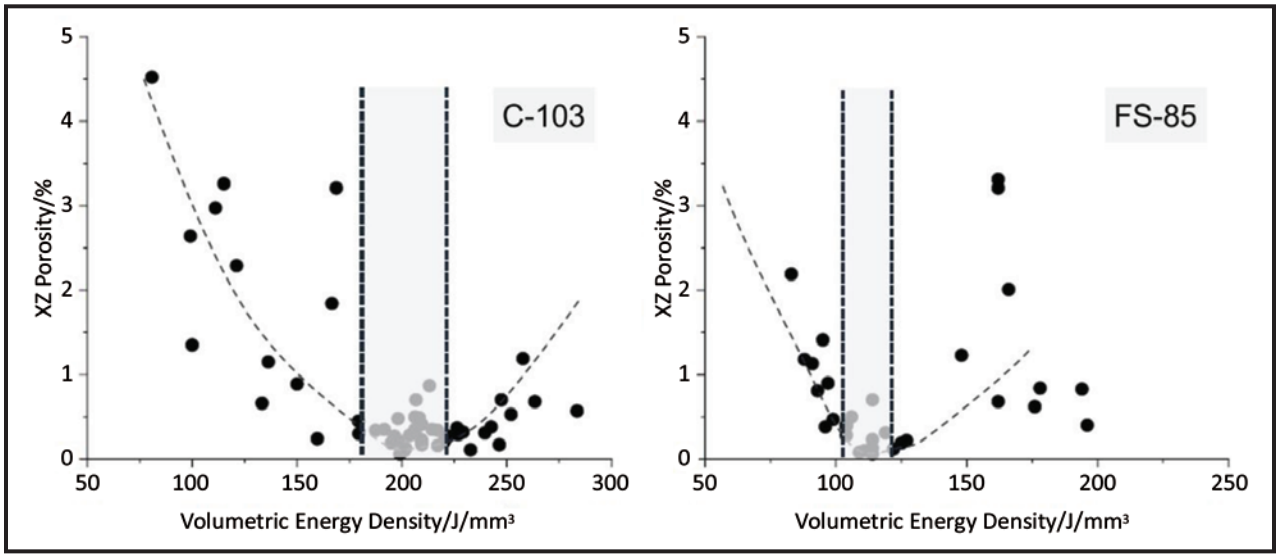

Figure 6. *Influence of energy input in the PBF-LB processing of C-103 and FS-85 in AM400. Determination of porosity from polished cross-sections of as-built test cubes*

BD, shows two characteristic features of AM parts, namely a relatively fine-grained morphology with crystallite sizes in the single digit micrometre scale (note that these are cross-sections of columnar grains, which possess a high aspect ratio) and melt pool boundaries, highlighted by white arrows. As a main feature, the element mapping shows a very homogeneous distribution of the elements, which is very different from the alloy particles used in the AM process. As evident from Figure 2 and Table II those exhibited dendritic structural features and variations in the chemical distribution of up to 7 wt.% for Nb and 5.5 wt.% for Ta and W. Although some minor fluctuations are visible along the melt pool boundaries in the AM-processed structure, these are in the range of < 0.5 wt.%. This is probably due to the very high cooling rates of 1–40 °C/µs in the PBF-LB process, which pre-

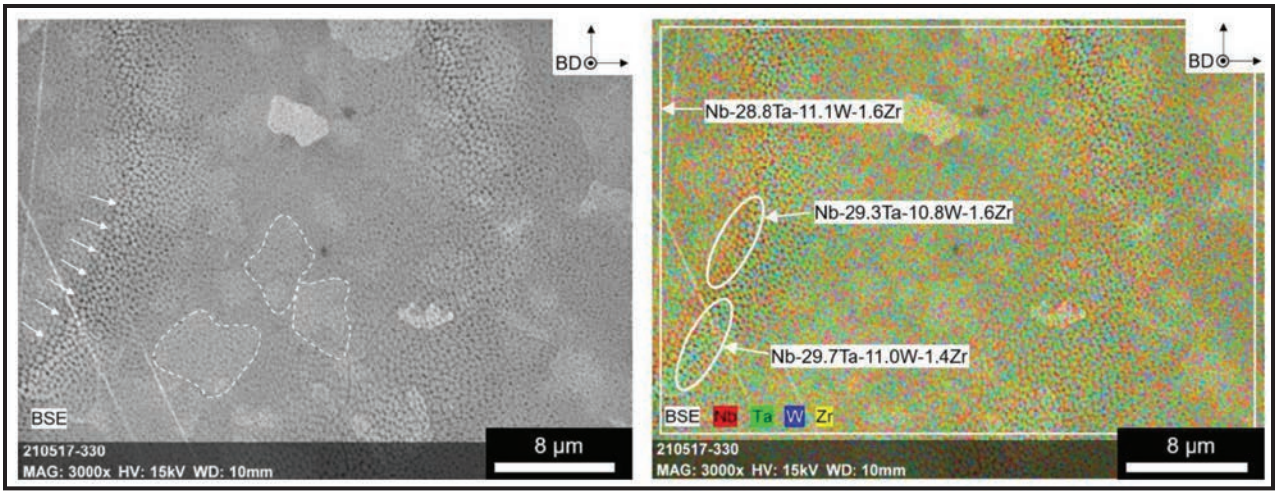

Figure 7. *Backscattered electron (BSE) image and corresponding element mapping of FS-85 processed by PBF-LB. White arrows highlight a melt pool boundary with chemical composition in the EDS mapping (left), dotted lines point out selected grain boundaries of cross-sections of columnar grains, oriented in the BD (perpendicular to the image plane).*

vent the melt from de-mixing during solidification.[24] In contrast, the inherent cooling rates during EIGA are not high enough to prevent segregation and consequently, dendritic structures form during solidification.

Infill Parameter Development Using Multi-Laser Renishaw AM500Q for Commercialization

Parameter development for building C-103 by PBF-LB in a protective Ar environment for commercial application was pursued in a multi-laser Renishaw AM500Q, equipped with four-fiber laser systems (ytterbium fiber lasers, p_{max} = 500 W, λ = 1080 nm). The set of parameters building the highest density C-103 cubes in the AM400 were used as starting parameter sets for parameter development in the AM500Q. Using the starting parameters, power, laser scan speed, and hatch spacing were varied to investigate the density produced from a range of VEDs in the AM500Q.

XZ porosity versus VED is presented in Figure 8, showing a processing window scan for C-103 in the AM500Q ranging 95 – 255 J/mm^{-3}. This window of operation was larger than that of C-103 in the AM400 (160 – 240 J/mm^{-3}), providing additional information about the correlation between types of defects and VED in the parameter development phases.

The optical density variation of all the parameters tested on AM500Q is illustrated in Figure 9. All 22 parameters plotted in the VED vs. XZ porosity graph in Figure 8 were computed using the images shown in Figure 9.

Variation of Optical Density Across the Build Plate

The stability of the build process for C-103 was investigated by manufacturing 52 cubes on the AM500Q across the entire build envelope to occupy as much area as possible of the 250 mm by 250 mm build space. The

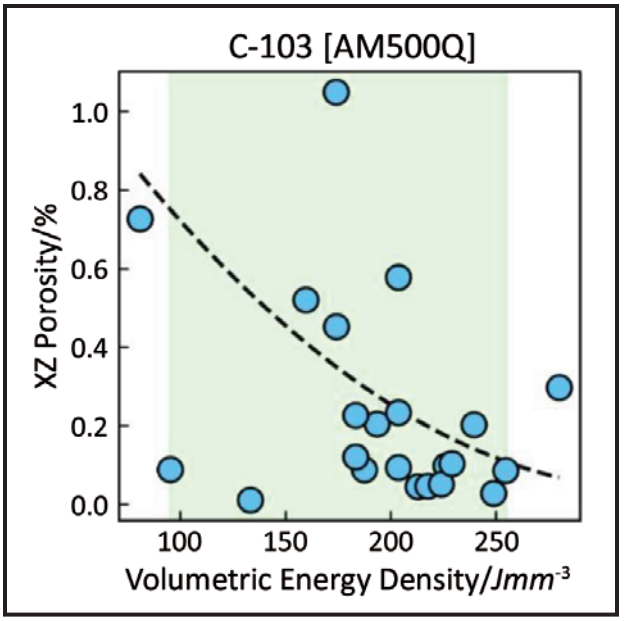

Figure 8. *Influence of energy input in the PBF-LB processing of C-103 in AM500Q. Determination of porosity from polished XZ cross section of as-built C-103 test cubes*

cubes were built with a single laser using the best four parameter sets determined in the build parameter development described above. Accordingly, VED in the range of about. 200–250 J/mm^3 were applied. The cubes were clustered into groups of four, with each parameter randomly assigned, to prevent systematic fluctuations in the measured densities. The assignment of the cubes is shown in Figure 10.

The results of the build plate variation study are graphically summarized in Figure 11. Their evaluation is carried out according to ASTM (WK77186) or the more stringent standards defined by Alloyed. Despite a

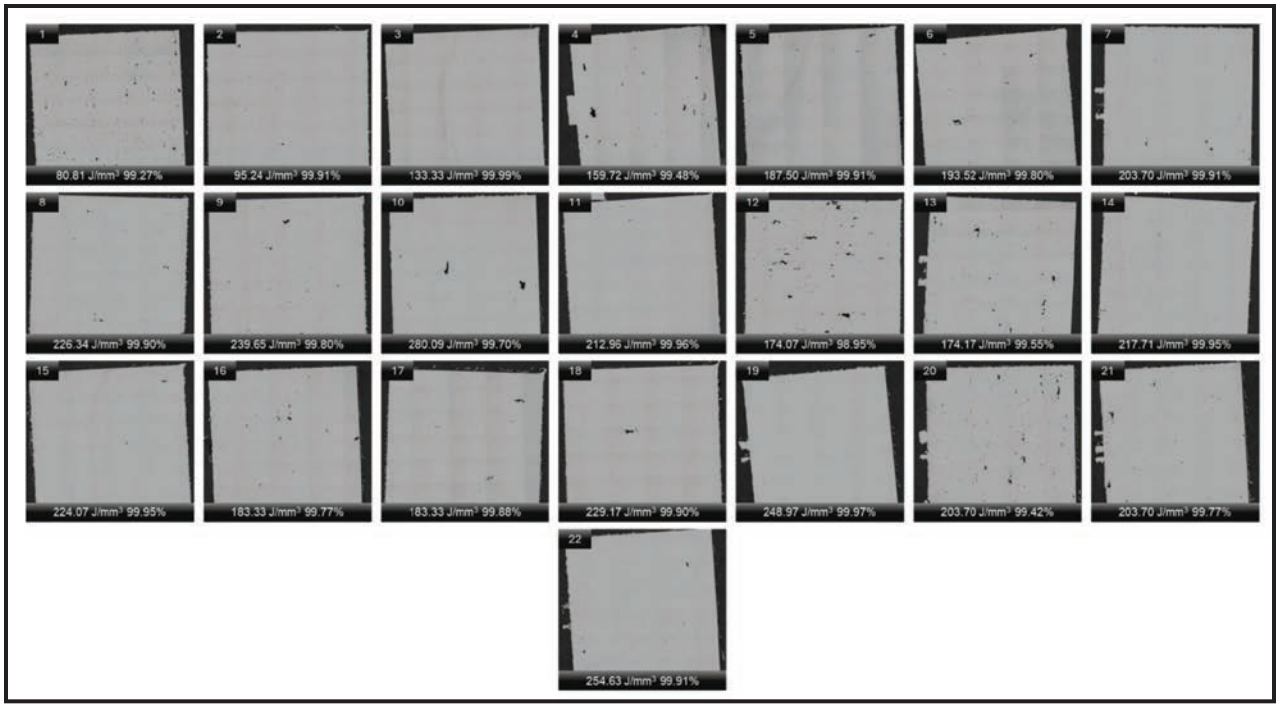

Figure 9. *Light microscopy images of polished of XZ cross sections of as-built C-103 test cubes using the AM500Q system, illustrating the influence of energy input in the PBF-LB processing on (relative) optical density*

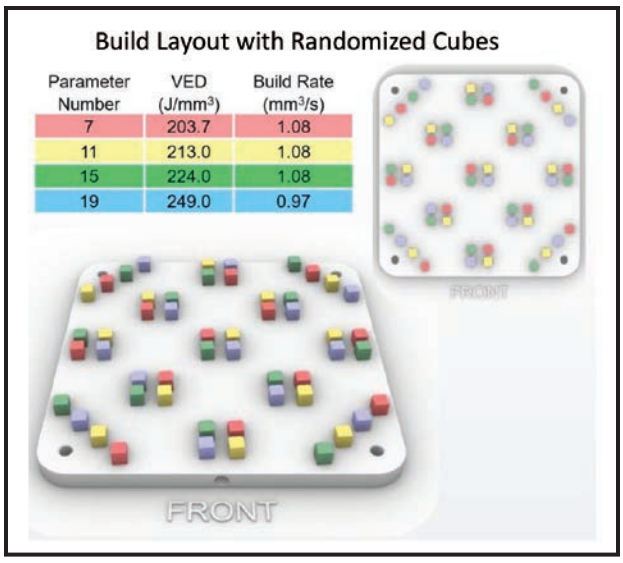

Figure 10. *Positioning and assignment of the test cubes on the build plate of the AM500Q system*

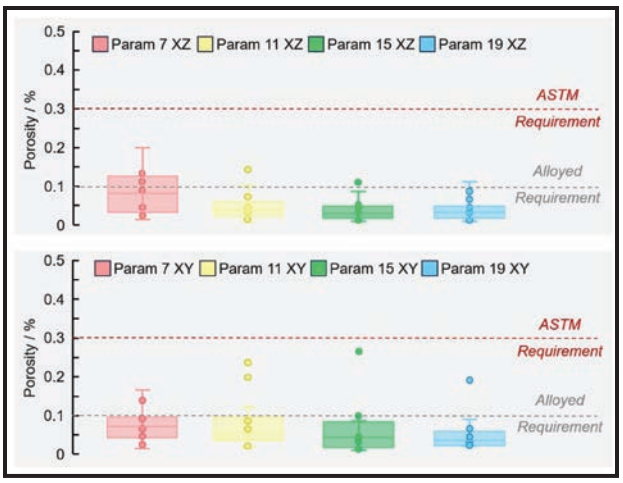

Figure 11. *XZ (top) and XY (bottom) optical densities using parameters 7, 11, 15 and 19 over 13 repetitions throughout the AM500Q build space (c.f. Figure 10). ASTM requirements are given for assessment purposes*

small number of outliers, especially in XY, all four parameters were successfully applied to manufacture specimens. In terms of porosity, they are clearly surpassing the ASTM requirements in the XY and XZ direction, i.e., having < 0.3 % porosity. This finding is essential to succeed at a commercial level as it will allow the utilization of all available space in the chamber to maximize the productivity per build. The few outliers seen in XY are most probably caused by stochastic spatter-induced defects that influence the density measurements in XY more significantly as these measurements are conducted over half the area of the XZ measurements.

Pre-Commercialization of the Additive Manufacturing of C-103 And FS-85 By Means of PBF-LB

To demonstrate the maturity of PBF-LB of niobium-base alloys C-103 and FS-85, demonstrator components were manufactured using the newly developed

parameters. These included several thrusters for in-space propulsion. Two, which are 53-mm in diameter and 100-mm in height, are shown in Figure 12. All thrusters manufactured were free of cracks or other macroscopic defects.

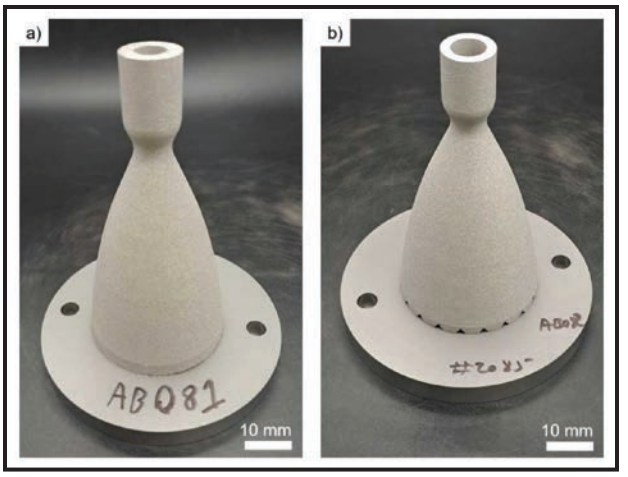

Figure 12. *Thrusters produced from FS-85 via PBF-LB F showing no evidence of macro-cracking. The thruster shown in b) additionally features inverted V-notch depowering holes*

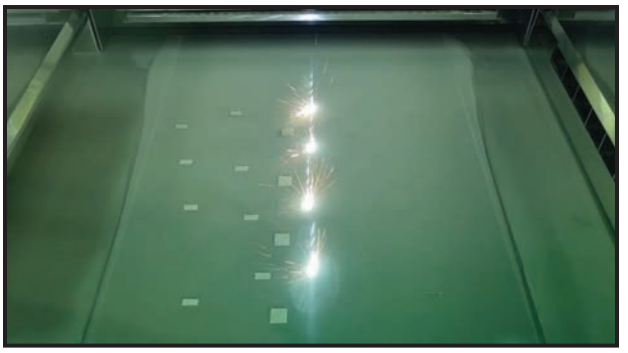

Figure 13. *An image of a build running on the AM500Q with all 4 lasers firing simultaneously*

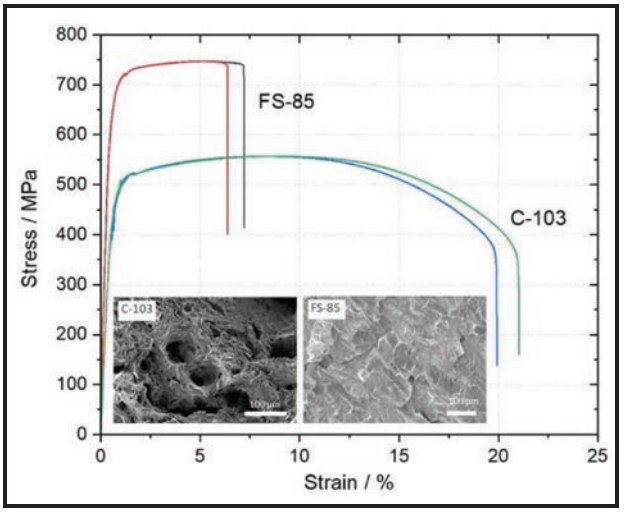

Figure 14. *Representative tensile stress–strain curves of the PBF-LB processed C-103 and FS-85 alloys in the as-built condition (single laser). The inserted SEM image of FS-85 represents a typical fracture site*

The previous builds were conducted using only one of the four lasers available in the AM500Q. This strategy was chosen to ensure reproducibility of all build jobs. To improve the productivity of the build process and shorten the process time, tests were carried out using all four laser systems simultaneously. The results of the mechanical tests on samples produced on the AM500Q shown subsequently are from samples produced in quad laser mode.

Mechanical and Structural Characterization of Additively Manufactured Parts

Additively manufactured FS-85 and C-103 were investigated for their strength and hardness at room temperature and elevated temperature up to 1,600 °C. Room temperature strength tests were performed according to ASTM E8. Rectangular blanks of dimension 55 by 10 by 10 mm^3 were machined into cylindrical dumbbell specimens with threads on either end. The samples were tested in tension in a 30 kN Instron tensile testing machine at a strain rate of 0.005 mm/mm/min. The stress/strain diagrams are provided in Figure 14.

FS-85 is significantly stronger than C-103. The corresponding yield strengths and ultimate strengths are approximately 659 and 750 MPa for FS-85 compared with 459 and 565 MPa for C103. The latter is in accordance with previously published UTS of additively manufactured C-103.[25] The elastic moduli were determined to be 137 and 95 GPa, respectively, indicating that FS-85 is considerably stiffer than C-103. On the other hand, C-103 is more ductile, as it has a notably higher strain to failure (stf) of 20–22 % compared with 6–7 % in FS-85. A comparison of all data is listed in Table III.

Compared with conventionally processed materials (Table III), the additively manufactured test specimens have higher strength but lower ductility. This is especially valid for AM processed FS-85 with 7% strain to failure, compared with 23% for conventionally processed material. The difference in ductility is reflected in the fracture behavior of FS-85 and C-103. The fracture surface of FS-85 (insert Figure 14) shows typical

TABLE III. MECHANICAL CHARACTERISTICS OF ADDITIVELY MANUFACTURED (AM) C-103 AND FS-85 SAMPLES, DETERMINED BY TENSILE STRENGTH TESTS PERFORMED ACCORDING TO ASTM E8 COMPARED WITH CONVENTIONALLY PROCESSED ALLOYS[26]

	C-103 (conv.)	C-103 (AM)	FS-85 (conv.)	FS-85 (AM)
Yield Strength (MPa)	296	462	485	659
Ultimate Strength (MPa)	420	557	570	747
Elastic Modulus (GPa)	90	95	140	140
Strain to Failure (%)	26	21	23	7

features of quasi-cleavage fracture—intergranular fracture that occurred along grain boundaries.[27] In contrast, the fracture surface of C-103 shows dimples and has a fibrous appearance.

Comparison of the Mechanical Performance of C-103 Prepared Using the AM500Q and AM400

To compare the mechanical performance of material produced using the two different systems, tensile specimens were produced in the XZ (building direction, BD) and XY (90° rel. BD) directions. These specimens had a gage length of 16 mm and a diameter of 4 mm. They were machined and tested according to ASTM E8 (specimen 4 type small cylindrical samples proportional to the standard) using a strain rate of 0.005 mm/mm/min until failure. The results of this testing are shown in Table IV.

Table IV shows a good level on consistency between the performance achieved on both systems. Material produced on the AM500Q shows both a slight reduction in yield stress and ultimate tensile stress. One possible explanation is a reduced level of residual stress left behind the continuous laser of the AM500Q when compared with the modulated AM400. The elongation measurements for all samples fall within margin of error considering the relatively small number of tests conducted. However, it is noted that XZ samples exhibit a lower ductility than XY samples due to the anisotropic grain structure produced by PBF-LB. The stress-strain diagrams of all the samples tested and mentioned in Table IV are shown in Figure 15.

TABLE IV. XY (90° REL. BD) AND XZ (IN BD) TENSILE PROPERTIES OF EACH 4 REPRESENTATIVE C-103 SPECIMENS PRODUCED USING THE AM400 (SINGLE LASER) AND THE AM500Q (FOUR-LASER SYSTEM), MEASURED ACCORDING TO ASTM E8 AT ROOM TEMPERATURE

Machine	Direction	Young's Modulus (GPa)	0.2% YS (MPa)	UTS (MPa)	Strain to Fracture (%)
AM400	XY	108.7	524	618	28.7
	XZ	107.4	513	598	27.1
AM500Q	XY	118.1	509	597	29.0
	XZ	104.2	489	579	25.9

Both alloys have also been investigated at higher temperatures up to 1,600 °C to evaluate their potential for service in high-temperature environments. The measurements were performed by means of Electro-Thermal Mechanical Testing (ETMT) using a 5 kN Instron® ETMT machine.[28,29] The setup of the equipment is shown in Figure 16.

Tensile tests were performed from room temperature up to 1,600 °C in an Ar atmosphere on miniaturized specimens having a cross-section of 2.0 by 1.0 mm^2 and a gauge length of 14 mm, with an overall length of 40 mm. The specimens were crafted through wire electrical discharge machining (EDM) and subsequently polished with 4000 grit silicon carbide paper to eliminate the EDM-induced recast layer and ensure uniform surface quality. An R-type thermocouple was affixed to the specimen's midpoint to monitor temperature during the tests. To mitigate experimental variability, each test was conducted in triplicate.

The strain-rate for the tensile testes conducted on the ETMT was maintained at 10^{-4}/s. For high temperature testing, specimens were heated using electrical resis-

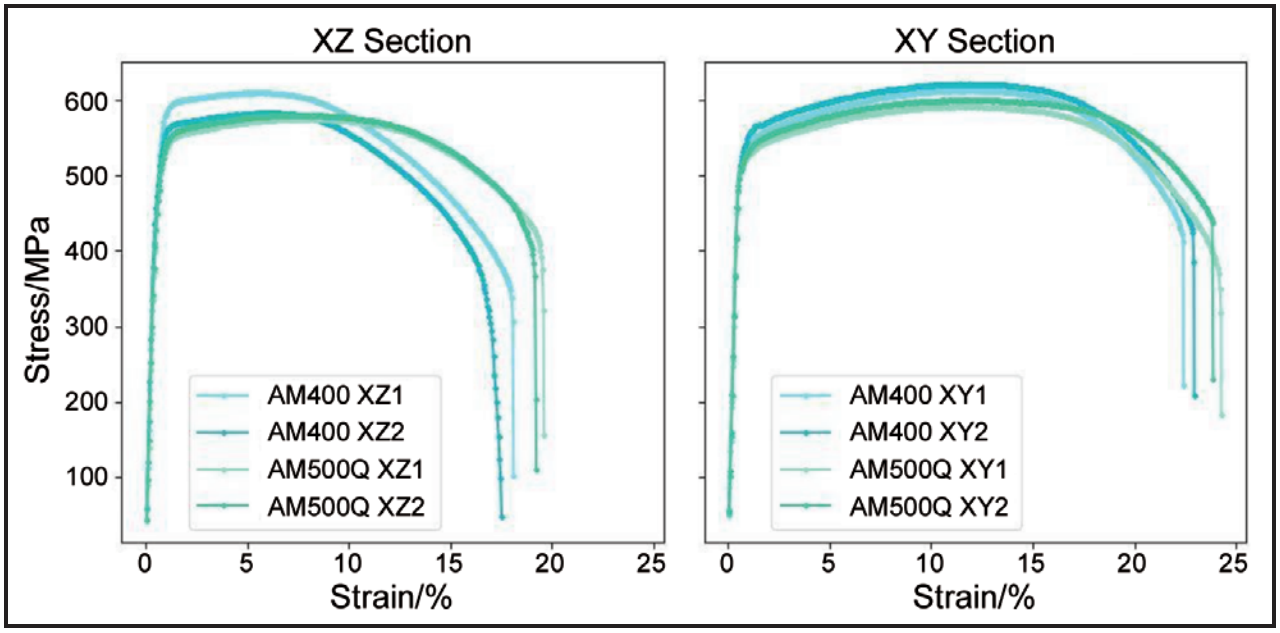

Figure 15. *Comparison of stress-strain behavior at room temperature for C-103 specimens produced using single laser Renishaw AM400 and a quad laser AM500*

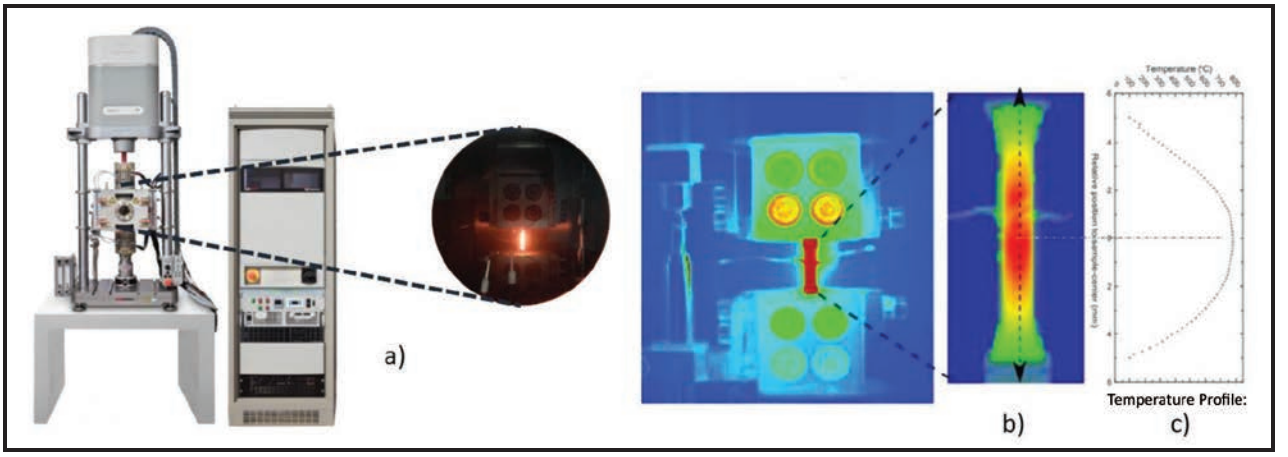

Figure 16. *a) Instron Electro-Thermal Mechanical Testing System (ETMT). ETMT was done up to 1,600 °C in Ar atmosphere. The target temperature was only reached in the central area of the sample (b). The temperature gradient across the entire sample is shown in (c)*

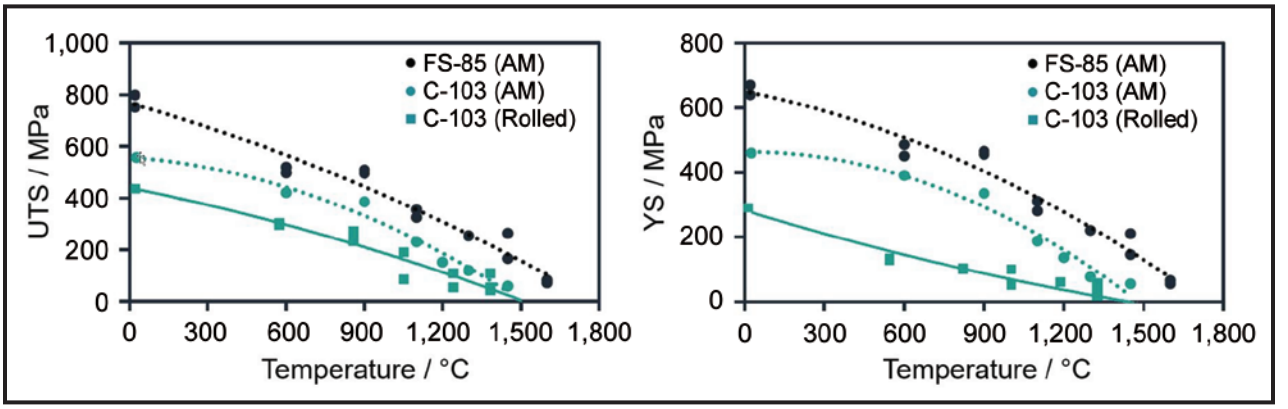

Figure 17. *Temperature dependent UTS (left) and YS (right) of PBF-LB manufactured C-103 and FS-85 alloys determined by ETMT and comparison with conventionally processed (rolled) C-103*

tance by passing a direct current through the specimen. This heating method results in a parabolic temperature distribution along the loading axis of the specimen, with the peak temperature achieved at the center. During high-temperature testing, the initial strain rate was controlled using a high-temperature extensometer, with an initial separation of 2 mm.

The results of the ETMT investigations are graphically presented in Figure 17. The most important findings are:

- FS-85 is clearly stronger than C-103 over the whole temperature range, starting from room temperature (the as-manufactured state) up to the final temperature. Even at 1,500 °C, when C-103 strength values approach 0, the UTS and YS of FS-85 are still in the range of approximately 220 MPa and 195 MPa, respectively.
- Additively manufactured C-103 is significantly stronger than the classically processed, rolled material. The measured strength values are 557 MPa vs. about. 420 MPa (UTS) and 462 MPa vs. 296 MPa (YS).
- As the temperature increases (above about 800 °C), the gap between UTS as well as YS of additively manufactured and rolled C-103 decreases. This is due to a coarsening of the additively manufactured microstructure and an associated loss in strength. Nevertheless, AM C-103 remains stronger than rolled C-103 over the whole temperature range, until the point of mechanical degradation is reached.

Investigation by means of EBSD shed further light on this issue. A comparison of the direction-dependent microstructure is provided in Figure 18.

A comprehensive macrostructural analysis was conducted on C-103 in its rolled, additive manufactured (built), and post-process heat-treated (1,900 °C/2 h/Ar; built-recrystallized) states. The microstructure of the rolled (and recrystallized) C-103 exhibited uniformly distributed, equiaxed grains when observed along both the XY and XZ planes, with an average grain size measured at 24 ±12 µm and 23 ±11 µm, respectively. The rolled specimen underwent a thermo-mechanical treatment involving 75% cold work at ambient temperature,

followed by a recrystallization anneal at 1,200 °C for one hour.

The microstructure of the built C-103 produced using an AM400 machine exhibited anisotropy, with a distinct melt-pool structure visible in the XZ plane. To mitigate this microstructural anisotropy, several heat-treatment trials were conducted on the as-built C-103 samples. Notably, achieving recrystallization in the as-built microstructure required elevated temperatures, as the absence of an adequate driving force hindered the process. Additionally, the higher oxygen content and lack of mechanical deformation compared with rolled material contributed to sluggish recrystallization kinetics at lower temperatures. The temperature required for recrystallization was significantly higher than the homologous temperature of 0.6 T_{mp}.

CONCLUSIONS

Niobium-base high-temperature alloys such as C-103 (Nb-10Hf-1Ti) and FS-85 (Nb-28Ta-10W-1Zr) are accessible using laser powder-bed-fusion (PBF-LB) of prealloyed powders. Such powders can be produced by electrode induction melting gas atomization (EIGA). The as-atomized powders must be refined by sifting and sieving to be adapted to the requirements of the additive manufacturing process applied. In this study, PBF-LB has initially been performed using a Renishaw AM400 system, equipped with a 1075 nm single fiber laser system. The systematic variation of the process parameters, particularly the volumetric energy density (VED) and the subsequent investigation of the porosity led to optimized process parameters for both C-103 and FS-85. Optical densities of the built specimens of > 99.9% could be achieved for either of the alloys. Tensile strength investigations of additively manufactured specimens showed that FS85 is significantly stronger than C-103. Yield strengths and ultimate strengths of 659 MPa and 750 MPa were observed for FS-85 compared with 459 MPa and 565 MPa for C-103. On the other hand, C-103 has a notably higher strain to failure (stf) of 20–22 % compared with 6–7 % in FS-85 and is thus more ductile. Tensile tests from room temperature up to 1,600 °C conducted on an Instron Electro-Thermal Mechanical Testing (ETMT) system gave valuable information on the applicability of C-103 and FS-85 alloys at elevated temperature. FS-85 is clearly stronger than C-103 over the entire temperature range. At 1,500 °C, when C103 strength values approach 0, UTS and YS of FS-85 are still 220 MPa and 195 MPa respectively.

Finally, it was shown that the process knowledge gained for Renishaw's AM400 single laser system can be transferred to the production scale with a four-laser AM500Q system. The influence of single (fiber) laser and the simultaneous use of four lasers on the density and mechanical properties of specimens in different positions on the build plate of the AM500Q system was investigated. Regardless of the positioning on the build plate samples with porosities < 0.1 % could be produced consistently. Investigations of the mechanical properties through tensile strength tests confirmed a high level of consistency between the performances achieved by both systems. Accordingly, there appear to be no obvious technical hurdles to scaling production of components made of C-103 or FS-85 using PBF-LB.

REFERENCES

1. C. Himmelblau, M. Kibrick, J. Runkle, A. Joshi, J. Wadsworth and J. Moncur, "Mechanical Properties of HIP Columbium C-103 Alloy", *Prog. Powder Metall.;* (United States) OSTI ID:5055443, 1984.
2. R.T. Torgerson, "Development and Evaluation of C-129Y (Cb-10W-10Hf-0.1Y) Columbium Alloy", NSA-19-011667, 1964.
3. R.G. Baggerly and R.T. Torgerson, "Evaluation of Cb-752, Columbium Alloy (Cb-10 percent W-2.5 percent Zr)", NSA-18-007203, 1963, https://doi.org/10.2172/4141837
4. R.H. Titran and R.W. Hall, "High-Temperature Creep Behavior of a Columbium Alloy", FS-85, National Aeronautics and Space Administration, 1965.
5. J.A. Horak and L.K. Egner, "Creep Properties of Nb-1Zr and Nb-1Zr-0.1 C", No. ORNL-6809, Oak Ridge National Lab, 1994.
6. M.G. Hebsur and R.H. Titran, "Tensile and Creep Rupture Behavior of P/M Processed Nb-base Alloy", WC3009, NASA Technical Memorandum 101954, 1988, https://ntrs.nasa.gov/citations/19890010000
7. L.J. Pionke and J.W. Davis, "Technical Assessment of Niobium Alloys Data Base for Fusion Reactor Applications", COO-4247-2 TRN: 80-007505, 1979, https://doi.org/10.2172/5419637
8. H. Inouye, "Niobium in High Temperature Applications", *Proc. Inter. Symp,* Metallurgical Society of AIME, 1984.
9. E.N. Sheftel and O.A. Bannykh, "Niobium-Base Alloys", *Int. J. of Refrac. Metals & Hard Mater,* 1993-1994, vol. 12, no.5, pp. 303–304, https://doi.org/10.1016/0263-4368(93)90038-H
10. V.V.S. Prasad, R.G. Baligidad and A.A. Gokhale, "Niobium and Other High Temperature Refractory Metals for Aerospace Applications", *Aerospace Materials and Material Technologies,* edited by N. Eswara Prasad and R.J.H. Wanhill, Indian Institute of Metals Series, 2016, https://doi.10.1007/978-981-10-21343_12
11. T. Griemsmann, A. Abel, C. Hoff, J. Hermsdorf, M. Weinmann and S. Kaierle, "Laser-based Powder Bed Fusion of Niobium with Different Build-up Rates", *Int. J. Adv. Manuf. Technol.,* 2021, vol. 114, pp. 305-317, https://doi.org/10.1007/s00170-021-06645-y
12. S. Candela, P. Rebesan, D. De Bortoli, S. Carmignato, F. Zanini, V. Candela, R. Dima, A. Pepato, M. Weinmann and P. Bettini, "Pure Niobium Manufactured by Laser-Based Powder Bed Fusion: Influence of Process Parameters and Supports on As-Built Surface Quality", *Int. J. Adv. Manuf. Technol.,* 2024, vol. 131, pp. 4469–4482, https://doi.org/10.1007/s00170-024-13249-9
13. F. Motschmann, R. Gerard and F. Gilles, "Purification of Selective Laser Melting Additive Manufactured Niobium for Superconducting RF-Applications Transactions on Applied Superconductivity", *IEEE* Transactions on Applied Superconductivity, 2019, vol. 29, no.5, pp. 1–5, https://doi.org/10.1109/TASC.2019.2900521
14. E. Martinez, L.E. Murr, J. Hernandez, X. Pan, K. Amato, P. Frigola. C. Terrazas, S. Gaytan, E. Rodriguez, F. Medina and R.B.

Wicker, "Microstructures of Niobium Components Fabricated by Electron Beam Melting", *Metallogr. Microstruct. Anal.,* 2013, vol. 2, pp. 183–189, https://doi.org/10.1007/s13632-013-0073-9
15. C.A. Terrazas, J. Mireles, S.M. Gaytan, P.A. Morton, A. Hinojos, P. Frigola and R.B. Wicker, "Fabrication and Characterization of High-purity Niobium using Electron Beam Melting Additive Manufacturing Technology", *Int. J. Adv. Manuf. Technol.,* 2016, vol. 84, pp. 1115–1126, https://doi.org/10.1007/s00170-015-7767-x
16. R. Dicks, F. Wang and X. Wu, The Manufacture of a Niobium/Niobium-silicide-based Alloy using Direct Laser Fabrication, *J. Mater. Proc. Techn.,* 2009, vol. 209, no. 4, pp. 1752–1757, https://doi.org/10.1016/j.jmatprotec.2008.04.042
17. J. Liao, Z. Wei, F. Yu, Y. Yu, H. Peng and J. Sha, "Microstructure and Fracture Behaviours of Nb-16Si Ultrahigh Temperature Alloy Fabricated by Laser Directed Energy Deposition", *Intermetallics*, 2023, vol. 157, p. 107874, https://doi.org/10.1016/j.intermet.2023.107874
18. https://www.icdd.com
19. J. Markhoff, M. Weinmann, C. Schulze and R. Bader, "Influence of Different Grained Powders and Pellets made of Niobium and Ti-42Nb on Human Cell Viability", *Mat. Sci. Eng. C,* 2017, vol. 73, pp. 756–766, https://doi.org/10.1016/j.msec.2016.12.098
20. C. Lauhoff, T. Arold, A. Bolender, M.W. Rackel, F. Pyczak, M. Weinmann, W. Xu, A. Molotnikov and T. Niendorf, "Microstructure of an Additively Manufactured Ti-Ta-Al Alloy using Novel Pre-alloyed Powder Feedstock Material", *Addit. Manuf. Manuf. Lett.,* 2023, vol. 6, p. 100144, https://doi.org/10.1016/j.addlet.2023.100144
21. P.A. Hooper, "Melt Pool Temperature and Cooling Rates in Laser Powder Bed Fusion", *Addit. Manuf.,* 2018, vol. 22, pp. 548–559, https://doi.org/10.1016/j.addma.2018.05.032
22. R. Acharya, J.A. Sharon and A. Staroselsky, "Prediction of Microstructure in Laser Powder Bed Fusion Process", *Acta Mat.,* 2017, vol. 124, pp. 360–371, https://doi.org/10.1016/j.actamat.2016.11.018
23. S.Y. Liu, H.Q. Li, C.X. Qin, R. Zong and X.Y. Fang, "The Effect of Energy Density on Texture and Mechanical Anisotropy in Selective Laser Melted Inconel 718", *Mater. Des.,* 2020, vol. 191, p.108642, https://doi.org/10.1016/j.matdes.2020.108642
24. P.A. Hooper, "Melt Pool Temperature and Cooling Rates in Laser Powder Bed Fusion", *Addit. Manuf.,* 2018, vol. 22, pp. 548-559, https://doi.org/10.1016/j.addma.2018.05.032
25. O. Mireles, O. Rodriguez, Y. Gao and N. Philips, "Additive Manufacture of Refractory Alloy C103 for Propulsion Applications", *Proc. AIAA Propulsion and Energy 2020 Forum,* 2020, pp. 1–13, https://doi.org/10.2514/6.2020-3500
26. C.C. Wojcik and W. Chang, "Thermomechanical Processing and Properties of Niobium Alloys", *Proc. Inter. Symposium on Niobium,* 2001, pp. 163–173.
27. A. Pineau, A.A. Benzerga and T. Pardoen, "Failure of Metals I: Brittle and Ductile Fracture", *Acta Mater.,* 2016, vol. 107, pp. 424–483, https://doi.org/10.1016/j.actamat.2015.12.034
28. https://www.instron.com/en/products/testing-systems/dynamic-and-fatigue-systems/high-temp-fatiguetesting-systems/etmt
29. B. Roebuck, M. Brooks and A. Pearce, "Good Practice Guide for Miniature ETMT Tests", *Good Practice Guide No.137,* National Physical Laboratory, 2016, http://eprintspublications.npl.co.uk/id/eprint/6874 ijpm